Advances in Engineering Software 72 (2014) 134–146

Contents lists available at SciVerse ScienceDirect

Advances in Engineering Software

journal homepage: www.elsevier.com/locate/advengsoft

Multiscale hydro-thermo-mechanical model for early-age and mature concrete structures

Libor Jendele [a,*], Vít Šmilauer [b], Jan Červenka [a]

[a] Červenka Consulting s.r.o., Na Hřebenkách 55, 150 00 Prague, Czech Republic
[b] Czech Technical University in Prague, Faculty of Civil Engineering, Thákurova 7, 166 29 Prague 6, Czech Republic

ARTICLE INFO

Article history:
Available online 4 June 2013

Keywords:
Cement hydration
Heat transport
Moisture transport
Multiscale model
Moisture diffusion
Concrete

ABSTRACT

Temperature and early-age mechanical properties in hydrating concrete structures present a significant risk for cracking, having a major impact on concrete durability. In order to tackle these phenomena, a multiscale analysis is formulated. It accounts for a high variety of cement properties, concrete composition, structure geometry and boundary conditions.

The analysis consists of two steps. The first step focuses on the evolution of moisture and temperature fields. An affinity hydration model accompanied with non-stationary heat and moisture balance equations are employed.

The second step contains quasi-static creep, plasticity and damage models. It imports the previously calculated moisture and temperature fields into the mechanical problem in the form of a staggered solution. The whole model has been implemented in the ATENA software, including also the effect of early-age creep, autogenous and drying shrinkage.

Validation on selected structures shows a good prediction of temperature fields during concrete hardening and a reasonable performance of the mechanical part.

1. Introduction

Thermal expansion, shrinkage and external restraints present a serious threat to concrete durability due to early-age cracking [1]. These problems may be investigated by means of virtual material and structure testing. Based on an accurate mathematical formulation of the underlying phenomena these models can assist in the prediction of structural deterioration. Sensitivity analysis and optimization present further extension of these multiscale models.

Extensive experimental research carried out in this area has already resulted in a number of precautions and recommendations incorporated in civil engineering guidelines and codes [2]. The formulation of numerical hydro-thermo-mechanical models followed historical evolution. The simplest models were formulated for the temperature evolution in hardening concrete under adiabatic curing conditions [3,4]. Recognizing a heterogeneous temperature distribution on the structural scale led to the development of multiscale models for temperature prediction [5,6] to cite a few. The most sophisticated models are based on chemo-mechanical coupling, adding optionally concrete creep, tensile failure with damage, plasticity or moisture transport [6–13]. These models are quite accurate and versatile, although they may suffer from a considerable number of input parameters being sometimes difficult to calibrate. Consequently, they are seldom used for routine engineering analyses.

This paper aims at developing a new simulation tool that can handle hydrating concrete in its complexity and heterogeneity. Emphasis is put on versatility, accuracy and rational simplicity, opening ways for wider engineering practice. A coupled multiscale approach was selected since it provides a robust modelling framework accommodating both material and structural scales. Now it is possible to account directly for cement properties, concrete composition, creep and shrinkage behaviour, structural topology, reinforcement and various boundary conditions.

The validation and verification present indispensable processes of any model. The international benchmark for crack control of reinforced concrete structures, known as ConCrack, see www.concrack.org, was chosen to illustrate the performance of the newly formulated multiscale model. It is worthy to review the results from 18 participating teams competed in the modelling of two reinforced beams using various software tools. A blind stage revealed that the maximum concrete core temperature in a RG8 experiment was predicted between 48 and 65 °C against the measured 55 °C. None of the competing teams reproduced correctly a dormant period and hydration kinetics strongly deviated. The results from the RG8 restrained shrinkage test revealed that only one model gave reasonable predictions for displacements. After

* Corresponding author. Tel.: +420 220610018; fax: +420 220612227.
E-mail addresses: libor.jendele@cervenka.cz (L. Jendele), vit.smilauer@fsv.cvut.cz (V. Šmilauer), jan.cervenka@cervenka.cz (J. Červenka).

0965-9978/$ - see front matter © 2013 Elsevier Ltd. All rights reserved.
http://dx.doi.org/10.1016/j.advengsoft.2013.05.002

the calibration stage, the majority of models were able to correct their predictions.

2. Formulation of hydro-thermo-mechanical model

Fig. 1 provides a flowchart of the developed multiscale hydro-thermo-mechanical model employing a staggered solution strategy. Firstly, moisture and heat transport analysis is carried out using a five-component model for concrete. Secondly, thermal and moisture fields are passed to the mechanical analysis of the structure. A weak coupling between hydro-thermal and mechanical parts is assumed, meaning that structural conditions in the mechanical model have no influence on the calculated hydro-thermal fields. The presented model has been implemented in the ATENA software [14].

2.1. Heat and moisture transport analysis

Heat and moisture analysis predicts the evolution of moisture and temperature fields. Both are used in the subsequent mechanical analysis for:

- Determination of the maximum temperature and its gradients.
- Calculation for thermal expansion and contraction strain.
- Accuracy enhancement of creep prediction models, e.g. the calculation of drying creep, drying shrinkage, the temperature effect on creep scaling.

2.1.1. Heat transport

The heat balance equation for non-stationary heat transport requires

$$\frac{\partial}{\partial t}(Q) = -\mathrm{div}(\bar{q}_T) \tag{1}$$

where Q is the total amount of heat accumulated in a unit volume of concrete in J/m^3 and $\bar{q}_T$ is a heat flux in J s^{-1} m^{-2}. A change of thermal energy occurs due to a temperature change and released hydration heat

$$\frac{\partial Q}{\partial t} = \frac{\partial Q_c}{\partial T}\frac{\partial T}{\partial t} + \frac{Q_h}{\partial t} = C_T\frac{\partial T}{\partial t} + \frac{\partial Q_h}{\partial t} \tag{2}$$

where Q_c is a heat gain or loss due to conduction in J/m^3, C_T is the heat capacity in J K^{-1} m^{-3}, Q_h is the total hydration heat released at the time t in J/m^3. The heat flux $\bar{q}_T$ is calculated via Fourier's law

$$\bar{q}_T = -\lambda\nabla(T) \tag{3}$$

where λ represents thermal conductivity in J s^{-1} m^{-1} K^{-1} for isotropic material. Substituting Eqs. (2) and (3) into Eq. (1) provides differential equation from which the unknown temperature field can be obtained.

2.1.1.1. Hydration heat. The affinity hydration model provides the framework for accommodating all stages of cement hydration and presents the core of the multiscale hydro-thermal formulation. It is accompanied by the calculation of released heat and consumed water during hydration stages. The degree of hydration $\alpha \in \langle 0,1\rangle$ can be approximated experimentally by the amount of liberated heat scaled to the potential hydration heat of cement, $Q_{h,pot}$, in J kg^{-1}

$$\frac{Q_h}{Q_{h,pot}} = \alpha \tag{4}$$

In the modelling, the degree of hydration is approximated by integrating the chemical affinity $\tilde{A}_{25}$. Expressing affinity at 25 °C has an advantage of easy scaling hydration kinetics with temperature while the other parameters inside the affinity model remain constants. The evolution of the degree of hydration under an arbitrary temperature T reads

$$\frac{\partial\alpha}{\partial t} = \tilde{A}_{25}\exp\left[\frac{E_a}{R}\left(\frac{1}{T_{25}} - \frac{1}{T}\right)\right] \tag{5}$$

where R is a gas constant 8.31441 J mol^{-1} K^{-1}, T is the current temperature in K, T_{25} is a reference temperature in K, and the activation energy E_a is approximately 40 kJ/mol, see [15].

Cervera et al. [16] developed an analytical form of the normalized affinity which was refined in [12]. A slightly modified formulation is proposed here

$$\tilde{A}_{25} = B_1\left(\frac{B_2}{\alpha_\infty} + \alpha\right)(\alpha_\infty - \alpha)\exp\left(-\eta\frac{\alpha}{\alpha_\infty}\right) \tag{6}$$

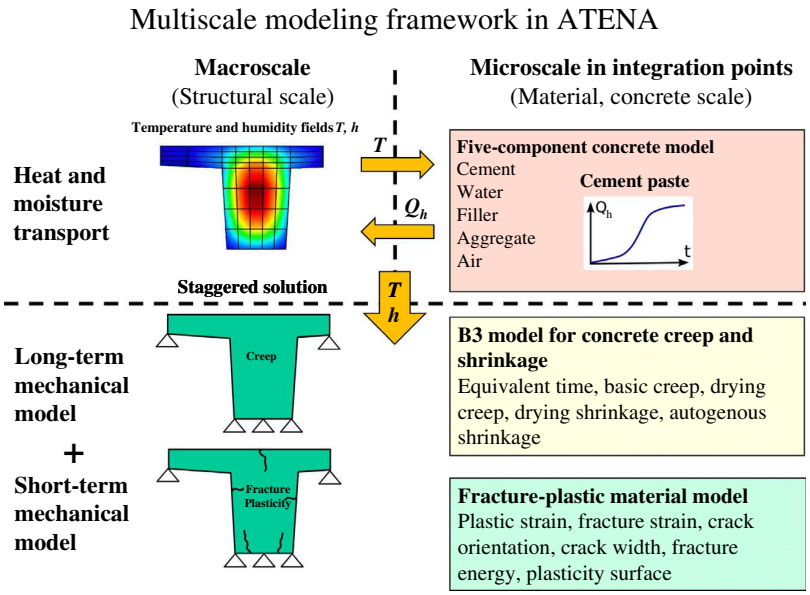

Fig. 1. Flowchart of the multiscale hydro-thermo-mechanical model.

where B_1 in s^{-1} and dimensionless B_2 are coefficients to be calibrated, α_∞ is the ultimate hydration degree and η represents the microdiffusion of free water through formed hydrates.

Gawin et al. [12], among others, added the effect of relative humidity on the hydration rate. The extension of (5) leads to

$$\frac{\partial \alpha}{\partial t} = \tilde{A}_{25}\beta_h \exp\left[\frac{E_a}{R}\left(\frac{1}{T_{25}} - \frac{1}{T}\right)\right] \tag{7}$$

$$\beta_h = \frac{1}{1 + (a - ah)^4} \tag{8}$$

where $\beta_h = \beta_h(h)$ accounts for the reduction of capillary moisture, h is the relative humidity and a is the material parameter, typically $a = 7.5$ [17]. The ultimate degree of hydration, α_∞, depends on the fineness of cement and also on available space for hydration products as follows [18]

Sealed curing

$$\alpha_\infty = \frac{w/c}{0.42}, \quad \alpha_\infty \leqslant 1 \tag{9}$$

Saturated curing

$$\alpha_\infty = \frac{w/c}{0.36}, \quad \alpha_\infty \leqslant 1 \tag{10}$$

where w/c is the water–cement ratio.

Substituting Eqs. (6) and (8) into (7) and (4) yields the final equation to predict the development of hydration heat. As it is impossible to express α evolution analytically from Eq. (7), the numerical integration takes place.

The model's parameters B_1, B_2, α_∞ and η need to be calibrated from isothermal calorimetry or other sophisticated hydration models. For example, the cement hydration model CEMHYD3D [19] allows us to account for the particle size distribution of cement, its chemical composition or water curing regime. Fig. 2 shows the performance of the affinity hydration model with regards to the CEMHYD3D model and isothermal calorimetry for cement paste as an example. The experiment was conducted at the Czech Technical University in Prague.

It is assumed that the hydration of cement paste is not influenced by the presence of aggregates in concrete. Upscaling hydration heat to concrete occurs through a known cement mass in concrete.

2.1.2. Heat capacity

Concrete is treated as a five-component material built up from aggregates, inert filler, water, cement and air. The contribution of these components to heat capacity follows the rule of mixtures

$$C_{concrete} = f_{aggregate}C_{aggregate} + f_{filler}C_{filler} + \widehat{C}_{paste} \tag{11}$$

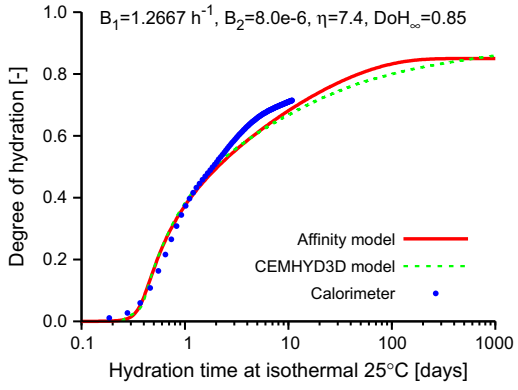

Fig. 2. Fitting the affinity hydration model and the CEMHYD3D model to the heat released from Portland cement CEM I 42.5R Mokrá, Czech Republic, at $w/c = 0.4$.

where $C_{concrete}$, $C_{aggregate}$, C_{filler} and $\widehat{C}_{paste}$ stand for the concrete, aggregate, filler and paste capacity (per unit volume) with corresponding volume fractions f. Bentz [4] studied the evolution of the paste heat capacity at 23 °C for w/c varying between 0.3 and 0.5. The heat capacity of hardening cement paste depends on the degree of hydration.

$$\widehat{C}_{paste} = (f_{cement}C_{cement} + f_{water}C_{water})(1 - 0.26(1 - \exp(-2.9\alpha))) \tag{12}$$

where C_{cement} in J m^{-3} K^{-1} is the unreacted cement heat capacity at the time zero and C_{water} in J m^{-3} K^{-1} is the capacity for capillary water [4]. The heat capacity of structural concrete normally spans the range between 800 and 1170 J kg^{-1} K^{-1} when expressed per kg of concrete [10].

2.1.2.1. Heat conductivity. The thermal conductivity of five-component fresh concrete is calculated from the well known Hashin–Shtrikman bounds (HS) and the Mori–Tanaka scheme (MT). Bentz [4] proposed using the arithmetical average of HS bounds for a fresh cement paste. In the presented model, the upscaling to the concrete level happens in the following hierarchical order:

1. Plain Portland paste = Unreacted cement + water (average of HS bounds).
2. Plain paste = Item 1. + filler (average of HS bounds).
3. Paste = Item 2. + air (Mori–Tanaka method).
4. Mortar, Concrete = Item 3. + aggregates (average of HS bounds).

Bentz [4] found that thermal conductivity for cement paste remains in the range of 0.9–1.05 W m^{-1} K^{-1} for an arbitrary degree of hydration, for both sealed and saturated curing conditions and for w/c spanning from 0.3 to 0.4. A reasonable approximation of thermal conductivity was obtained by HS bounds averaging, intermixing capillary water 0.604 W m^{-1} K^{-1} together with unreacted cement 1.55 W m^{-1} K^{-1} [4]. This is the first step in the homogenization. When calculating the thermal conductivities of two phases such that $\lambda_1 < \lambda_2$, the upper and lower HS bounds are derived

$$\lambda_{lower} = \lambda_1 + \frac{3f_2\lambda_1(\lambda_2 - \lambda_1)}{3\lambda_1 + f_1(\lambda_2 - \lambda_1)}$$
$$\lambda_{upper} = \lambda_2 + \frac{3f_1\lambda_2(\lambda_1 - \lambda_2)}{3\lambda_2 + f_2(\lambda_1 - \lambda_2)} \tag{13}$$

The homogenization then yields

$$\text{Average of HS bounds} \quad \lambda_{hom} = \frac{\lambda_{lower} + \lambda_{upper}}{2}$$
$$\text{MT method} \quad \lambda_{hom} = \lambda_{upper} \tag{14}$$

The second homogenization step combines cement paste with filler, which is further upscaled considering entrapped/entrained air. Due to a small volume of air in fresh structural concrete (around 5%), the Mori–Tanaka scheme is more suitable and coincides with the upper HS bound solely. The fourth homogenization yields the effective thermal conductivity for fresh concrete. It is well known that the aggregate conductivity and its volumetric fraction in the mixture strongly influence the concrete conductivity; for example granite lies between 1.7 and 4.0 W m^{-1} K^{-1} [20]. Hardened mature concrete yields values between 0.85 and 3.5 W m^{-1} K^{-1} [2]. Thermal conductivity for air in a pore is assumed 0.035 J(m s K)$^{-1}$.

Fig. 3 summarizes thermal conductivities for ordinary hardened concrete depending on the concrete unit mass and saturation conditions. It presents results according to Neville [2] and the Czech ČSN 731208 standard. The latter considers 1.5 W m^{-1} K^{-1} for dry concrete and 1.7 W m^{-1} K^{-1} for water-saturated concrete.

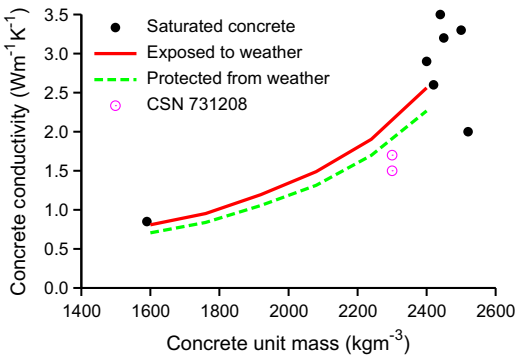

Fig. 3. Thermal conductivity of concrete according to Neville [2] and the Czech ČSN 731208 standard.

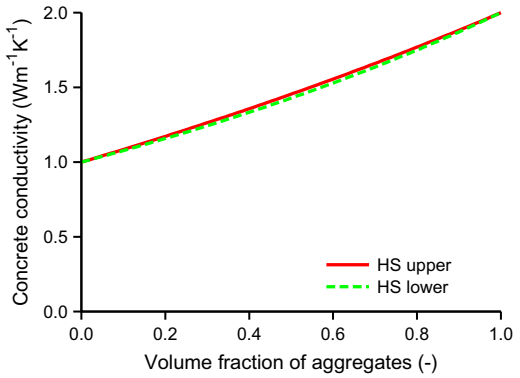

Fig. 4. Predicted thermal conductivity of concrete from HashinShtrikman bounds.

To elucidate the thermal effect of aggregates, let us consider a binding matrix with $\lambda_{binder} = 1.0\ \mathrm{W\,m^{-1}\,K^{-1}}$ and an aggregate with $\lambda_{aggregate} = 2.0\ \mathrm{W\,m^{-1}\,K^{-1}}$. The volume fraction of aggregates runs from 0 to 1. Fig. 4 shows that the lower and upper HS bounds are close to each other and averaging the bounds provides a reasonable approximation.

It is well known that the concrete thermal conductivity decreases at later times by about 20–30% from the initial fresh state. Ruiz et al. [21] approximated such a behaviour and the same relationship is also used in our model

$$\lambda_{concrete} = \lambda_{concrete,0}(1.0 - 0.248\alpha) \tag{15}$$

where $\lambda_{concrete,0}$ is the conductivity of fresh concrete obtained from the four-step homogenization.

2.1.3. Moisture transport

The presented formulation extends the work of Kuenzel [22]. It makes no difference between transportable liquid water and water vapour and it is suitable for problems with dominating diffusion and negligible convection. The governing equation for moisture transport in a unit volume reads

$$\frac{\partial w}{\partial t} + \frac{\partial w_h}{\partial t} = -\mathrm{div}(\bar{q}_h) \tag{16}$$

where w is the moisture content at the current time t in $\mathrm{kg\,m^{-3}}$, w_h stands for the moisture amount consumed by hydration in $\mathrm{kg\,m^{-3}}$, $\bar{q}_h$ represents the moisture flux in $\mathrm{kg\,m^{-2}\,s^{-1}}$. The time derivative of w is calculated as $\frac{\partial w}{\partial t} = C_h \frac{\partial h}{\partial t}$, in which C_h is the concrete moisture capacity in $\mathrm{kg\,m^{-3}}$ and h is relative humidity. The moisture flux is computed as

$$\bar{q}_h = -D_h \nabla h \tag{17}$$

where ∇h is a gradient of relative humidity and D_h is molecular diffusion coefficient, representing the sum of liquid water and water vapour in $\mathrm{kg\,m^{-1}\,s^{-1}}$, see Eq. (22).

2.1.3.1. Water consumption due to hydration. Experimental evidence shows that complete hydration of 1 kg high-alite cement powder consumes approximately 0.23 kg of water, i.e $Q_{w,pot} = 0.23$ [2]. It is expressed in units kg of water per kg of cement powder. This amount of water is often termed as chemically bound or non-evaporable. Taking a linear dependence of the water consumption w_h due to hydration on the degree of hydration α, the water sink term reads

$$w_h = Q_{w,pot} c \alpha \tag{18}$$

where c stands for the mass of cement in $1\ \mathrm{m^3}$ of concrete.

2.1.3.2. Moisture capacity of concrete. A simple constitutive law based on Kuenzel [22] is used to calculate the moisture capacity of concrete in $\mathrm{kg\,m^{-3}}$

$$w = w_f \frac{(b-1)h}{b-h} \tag{19}$$

where w_f in $\mathrm{kg\,m^{-3}}$ is free water saturation and b is a dimensionless approximation factor, which must always be greater than one. It can be determined from w_f and the water content w_{80} at a relative humidity $h = 0.80$ by substituting the corresponding numerical values into Eq. (19)

$$b = \frac{h(w_f - w_{80})}{w_f h - w_{80}} \tag{20}$$

The moisture capacity, C_h in $\mathrm{kg\,m^{-3}}$, is calculated as a derivative of moisture content with respect to h

$$C_h = \frac{\partial w}{\partial h} = \frac{w_f (b-1) b}{(b-h)^2} \tag{21}$$

2.1.4. Moisture diffusion

The moisture transport is formulated for a diffusion problem, which is applicable for dense concrete with mutually unconnected capillary pores. Hence, moisture convection through pores driven by water pressure is inhibited. The isotropic total moisture diffusivity D_h used in Eq. (17), is calculated as a sum of the water D_h^w and the water-vapour D_h^{wv} diffusivity

$$D_h = D_h^w + D_h^{wv} \tag{22}$$

The water liquid diffusivity D_h^w is calculated

$$D_h^w = D_w^w \frac{\partial w}{\partial h} \tag{23}$$

where the water diffusivity D_w^w in $\mathrm{m^2\,s^{-1}}$ is approximated [22]

$$D_w^w = \frac{3.8\ A^2 1000^{\left(\frac{w}{w_f}-1\right)}}{(w_f)^2} \tag{24}$$

with A being the water absorption coefficient in $\mathrm{kg\,m^{-2}\,s^{-0.5}}$, depending on a particular concrete mix. The water vapour permeability is computed from the water vapour pressure-driven diffusivity D_p^{wv} in $\mathrm{kg\,m^{-1}\,s^{-1}\,Pa^{-1}}$

$$D_p^{wv} = \frac{\delta}{\mu} \tag{25}$$

where μ is the water vapour diffusion resistance factor, and δ is the vapour diffusion coefficient in air in $\mathrm{kg\,m^{-1}\,s^{-1}\,Pa^{-1}}$ [22]

Table 1
Parameters for hydro-thermal simulations.

Parameter/experiment	Paste w/c = 0.25	Paste w/c = 0.50	Oparno bridge w/c = 0.425	RG8 ConCrack w/c = 0.4625
Cement mass (kg m^{-3})	1784	1234	409.45	400 (320)
Initial water mass (kg m^{-3})	446	617	178.0	185
Filler mass (kg m^{-3})	–	–	85.74	0 (80)
Aggregate mass (kg m^{-3})	–	–	1785	1765
Filler density (kg m^{-3})	–	–	2380	1400
Aggregate density (kg m^{-3})	–	–	2829	2620
Heat capacity of filler (J m^{-3} K^{-1})	–	–	2.377e+6	0.98e+6
Heat capacity of aggregates (J m^{-3} K^{-1})	–	–	2.377e+6	2.201e+6
Thermal conductivity of filler (J h^{-1} m^{-1} K^{-1})	–	–	4320	2160
Thermal conductivity of aggregates (J h^{-1} m^{-1} K^{-1})	–	–	8640	11520
Hydration model parameter B_1 (h^{-1})	1.8	0.9744	0.9744	1.8
Hydration model parameter B_2 (–)	3.52e−4	7.0e−4	7.0e−4	1.0e−5
Hydration model parameter α_∞ (–)	0.50	0.85	0.85	0.90
Hydration model parameter η (–)	4.6	6.7	6.7	7.0
Water mass at 80% rel. humidity w_{80} (kg m^{-3})	250	300	40	80
Cement density (kg m^{-3})	3220	3220	3220	3170
Water density (kg m^{-3})	1000	1000	1000	1000
Heat capacity of cement (J m^{-3} K^{-1})	2.415e+6	2.415e+6	2.415e+6	2.378e+6
Heat capacity of water (J m^{-3} K^{-1})	4.180e+6	4.180e+6	4.180e+6	4.180e+6
Thermal conductivity of cement (J h^{-1} m^{-1} K^{-1})	5580	5580	5580	5580
Thermal conductivity of water (J h^{-1} m^{-1} K^{-1})	2174	2174	2174	2174
Thermal conductivity of filler (J h^{-1} m^{-1} K^{-1})	–	–	4320	2160
Potential hydration heat $Q_{h,pot}$ (J kg^{-1})	509217	509217	509217	498200
Activation energy (J mol^{-1})	38300	38300	38300	38300
Parameter A for hydration rate decrease (–)	7.5	7.5	7.5	7.5
Chemically bound water $Q_{w,pot}$ (kg kg^{-1})	0.24	0.24	0.24	0.24
Water absorption coefficient A (kg m^{-2} h$^{-0.5}$)	0.6	0.6	0.6	0.6
Diffusion resistance factor μ (–)	210	210	210	210

$$\delta = \frac{0.00002306 p_a}{\frac{R}{M_w}(T+273.15)p_a}\left(\frac{T+273.15}{273.15}\right)^{1.81} \doteq 1.944E-12(T+273.15)^{0.81} \quad (26)$$

with the atmospheric pressure p_a = 101325 Pa, the universal gas constant R = 8.31441 J mol^{-1} K^{-1} and the molar mass of water M_w = 0.01801528 kg mol^{-1}. μ depends on a particular concrete mix and is given in Table 1.

Since the relative humidity h is the primary variable used to analyze moisture transport, D_p^{wv} must be transformed to D_h^{wv}

$$D_h^{wv} = D_p^{wv}\frac{\partial p}{\partial h} = D_p^{wv}\frac{\partial(p_{sat}h)}{\partial h} = D_p^{wv}p_{sat} \quad (27)$$

The pressure of saturated water vapour employs an empirical relationship in Pa [22]

$$p_{sat} = 611e^{\left(\frac{aT}{T_0+T}\right)}\ (\text{Pa}) \quad (28)$$

where T is temperature in °C and the remaining parameters are $T \geqslant 0$:T_0 = 234.18 °C, a = 17.08; $T < 0$: T_0 = 272.44 °C, a = 22.44.

2.2. Mechanical analysis

Mechanical analysis complements the hydro-thermal analysis, see Fig. 1. Separation into short-term and long-term material behaviour is the crucial feature of the presented formulation. While the short-term model provides short-term material response at a fixed particular time, the long-term model accounts for time-dependent phenomena such as concrete creep. Hence, at each time step, the long-term material model is used first to calculate actual material parameters and these are subsequently employed in the short term model to calculate final material response.

The coupling between heat/moisture analysis and mechanical analysis occurs via integration points. The meshes for both transport and mechanical problems can be different since the moisture and temperature fields are imported using the isoparametric interpolation. The presented model also supports geometric nonlinearity, allowing large displacements and large rotations [23].

2.2.1. Long-term material model

The time-dependent evolution of creep and shrinkage strains are incorporated via the Stieltjes integral [24]

$$\varepsilon(t) = \int_0^t \Phi(t,t')d\sigma(t') + \varepsilon^0(t) \quad (29)$$

where $\sigma(t)$ is the stress at the time t, $d\sigma(t')$ represents the stress increment, $\varepsilon^0(t)$ stands for material swelling/shrinkage at the time t taking into account thermal strains, autogenous shrinkage and drying shrinkage, $\Phi(t,t')$ is the compliance function of concrete creep, t is actual time and t' is time at the beginning of loading.

Eq. (29) represents the formulation for linear creep, which is valid up to about 60% of the concrete strength in compression. However, the simulation of very young concrete with high autogeneous shrinkage and external restraint means that tensile strength is comparable with tensile stress. In such a particular case, concrete creep becomes essentially nonlinear and stress relaxation is stronger than predicted. In this regard, early-age simulations tend to predict a slightly worse scenario for the crack development.

Eq. (29) is integrated in time by the step-by-step method (SBS) in which the original material compliance function is replaced by the Dirichlet series [25,26]. Knowing stress and strain at time t, their values at the time $t + \Delta t$ are calculated as follows [26]

$$\Delta\bar{\sigma}_t = \tilde{\mathbf{E}}_t(\Delta\bar{\varepsilon}_t - \Delta\tilde{\bar{\varepsilon}}_t) \quad (30)$$

$$\bar{\varepsilon}_{t+\Delta t} = \bar{\varepsilon}_t + \Delta\bar{\varepsilon}_t \quad (31)$$

$$\bar{\sigma}_{t+\Delta t} = \bar{\sigma}_t + \Delta \quad (32)$$

where $\bar{\sigma}_{t+\Delta t}$ and $\bar{\varepsilon}_{t+\Delta t}$ are total stress and total strain. Similarly, $\Delta\bar{\sigma}_t$ is stress and $\Delta\bar{\varepsilon}_t$ is overall strain increment at the time Δt, $\Delta\tilde{\bar{\varepsilon}}_t$ is inelastic strain increment to capture the creep history such as shrinkage and $(\Delta\bar{\varepsilon}_t - \Delta\tilde{\bar{\varepsilon}}_t)$ represents mechanical strain increment. $\tilde{\mathbf{E}}_t$ is the time adjusted material stiffness matrix [14,26]. Any consti-

tutive model for prediction of creep and shrinkage can be used for this type of analysis, e.g. the B3 model [27].

Creep and shrinkage of concrete heavily depends on humidity and temperature conditions. The effect of the variable temperature $T(t)$ is projected to the creep prediction model by using so-called equivalent time values $t_e(T,t)$. The creep prediction material law is normally calibrated for a constant reference temperature T_{ref}. In case of variable temperature conditions $T(t)$, the temperature adjusted predictions are obtained by the same models, whereby all real times t are replaced by their equivalent times t_e. This strategy is described in Section 1.7.2 in [27].

Each structural material point has an individual temperature history, resulting in unique equivalent time, creep and shrinkage functions. However, as the difference between the histories in adjacent material points are often negligible, these points can be grouped together and can share an average temperature. This technique significantly reduces the number of models' instances and speeds up the solution.

2.2.2. Short-term material model

The short-term material model accounts for all nonlinear behaviour due to crack development, material softening/hardening, fracture, plasticity, etc. It has been published in details in [14,28], and thus only a brief description is given here to show its overall concept and its link to the Long-term material model from Section 2.2.1.

Stress–strain behaviour strongly depends on current material conditions in each material point. The incremental formulation considers previous history. It uses several time-dependent variables, such as Young's modulus, compliance function of creep, inelastic strains, compressive and tensile strengths, which are computed, for a particular current and loading time t, t' and time increment Δt, by the Long-term material model from Section 2.2.1. For more details see also [14,26], and a creep prediction model such as [27].

Note that in this section all the time-related indices are stripped away in order to simplify the notation.

The short-term material model formulation is based on the decomposition of the strain vector into elastic $\bar{\varepsilon}_e$, plastic $\bar{\varepsilon}_p$ and fracturing $\bar{\varepsilon}_f$ strains [29], which for the incremental nonlinear solution can be written in the rate form as

$$\dot{\bar{\varepsilon}} = \dot{\bar{\varepsilon}}_e + \dot{\bar{\varepsilon}}_p + \dot{\bar{\varepsilon}}_f \tag{33}$$

The stress evolution is described by the formula

$$\dot{\bar{\sigma}} = \mathbf{E}(\dot{\bar{\varepsilon}} - \dot{\bar{\varepsilon}}_p - \dot{\bar{\varepsilon}}_f) \tag{34}$$

In the above $\mathbf{E}$ is abbreviated notation for $\bar{\mathbf{E}}_t$ from Eq. (30) and the two unknown strain vectors are defined as:

$$\dot{\bar{\varepsilon}}_f = \frac{\mathbf{E}}{\mathbf{E} + \mathbf{T}^{\mathrm{T}}\mathbf{E}_f\mathbf{T}}(\dot{\bar{\varepsilon}} - \dot{\bar{\varepsilon}}_p) \tag{35}$$

$$\dot{\bar{\varepsilon}}_p = \dot{\lambda}_p \bar{m}, \quad \dot{\lambda}_p = \frac{\bar{n}^{\mathrm{T}}\mathbf{E}(\dot{\bar{\varepsilon}} - \dot{\bar{\varepsilon}}_f)}{\bar{n}^{\mathrm{T}}\mathbf{E}\bar{m} - H_p}, \quad \bar{n} = \frac{\partial F_p}{\partial \bar{\sigma}}, \quad \bar{m} = \frac{\partial G_p}{\partial \bar{\sigma}} \tag{36}$$

Eq. (36) represents the fracturing model, which takes into account the development of tensile cracks, while the Eq. (37) corresponds to the plasticity model for the modelling of compressive concrete failure. These two equations are not independent and must be solved by an iterative algorithm, which is described in detail in [28].

In the fracturing model, Eq. (36), the fracturing strain $\dot{\bar{\varepsilon}}_f$ is calculated from the Eq. (35), where $\dot{\bar{\sigma}}$ is replaced by the stress in the cracks as defined in Eq. (38). $\mathbf{T}$ is the strain transformation matrix for transforming the strain vector from the global coordinate system into the local coordinate system aligned with cracks in concrete, and $\mathbf{E}_f$ is the stiffness matrix for the cracks. In the present model, maximum three orthogonal cracks can be modelled at each point and the matrix $\mathbf{E}_f$ has the following form

$$\dot{\bar{\sigma}}' = \mathbf{E}_f\dot{\bar{\varepsilon}}'_f, \quad \mathbf{E}_f = \begin{bmatrix} {}^1E_f & 0 & 0 & & & \\ 0 & {}^2E_f & 0 & & \mathbf{0} & \\ 0 & 0 & {}^3E_f & & & \\ & & & {}^{12}E_f & 0 & 0 \\ & \mathbf{0} & & 0 & {}^{23}E_f & 0 \\ & & & 0 & 0 & {}^{13}E_f \end{bmatrix} \tag{37}$$

where the prime indicates the stress and strain quantities in the local coordinate system in cracked concrete. The individual components of the matrix $\mathbf{E}_f$ are calculated by Eq. (39) using the softening evolution law (see Fig. 5) for the tensile strength f_t, which is a function of the crack opening displacement w_t. The crack band method of Bažant and Oh is used [30], which allows to relate the crack opening displacement w_t to the fracturing strains $\bar{\varepsilon}_f$ through the crack band size L_T (Fig. 5). The shear components ${}^{ij}E_f$ of the matrix $\mathbf{E}_f$ are assumed to be dependent on the corresponding normal components and on the multiplier s_F, which is assumed to be an input material parameter.

$${}^iE_f = \frac{\partial f_t({}^iw_t)}{\partial w}L_T, \quad {}^{ij}E_f = s_F \min({}^iE_f, {}^jE_f), \quad {}^iw_t = {}^i\varepsilon_f L_T \tag{38}$$

The elements of the transformation matrix $\mathbf{T}$ are gradually calculated at the onset of cracking in each of the three material direction. This corresponds to the fixed crack model, when the crack direction is fixed after the initiation. On the other hand, if the matrix $\mathbf{T}$ is recalculated for each step based on direction of the current principal strains, a rotated crack model is recovered. It should be also noted that evaluation of the fracturing model, i.e. the Eqs. (36) and (39) requires an iterative algorithm since $\mathbf{E}_f$ depends on $\bar{\varepsilon}_f$. This algorithm is described in detail in [28].

In the plasticity model, Eq. (37), the plastic strain rate $\dot{\bar{\varepsilon}}_p$ is calculated from the consistency condition. λ_p is the plastic multiplier, and $\bar{n}$ and $\bar{m}$ are stress derivatives of the plastic and potential surface respectively. The plastic surface F_p is defined by the three-parameter criterion, (f_c, f_t, e), according to Menetrey and Willam [32] (Fig. 6)

$$F_p = \left[\sqrt{1.5}\frac{\rho}{\widehat{f}_c}\right]^2 + m\left[\frac{\rho}{\sqrt{6}\widehat{f}_c}r(\theta,e) + \frac{\xi}{\sqrt{3}\widehat{f}_c}\right] - c = 0 \tag{39}$$

where

$$m = 3\frac{\widehat{f}_c^2 - f_t^2}{\widehat{f}_c f_t}\frac{e}{e+1}$$

$$r(\theta,e) = \frac{4(1-e^2)\cos^2\theta + (2e-1)^2}{2(1-e^2)\cos\theta + (2e-1)[4(1-e^2)\cos^2\theta + 5e^2 - 4e]^{\frac{1}{2}}} \tag{40}$$

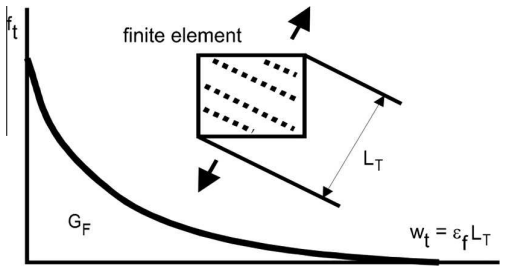

Fig. 5. Crack opening law Hordijk [30] and crack band L_T definition,

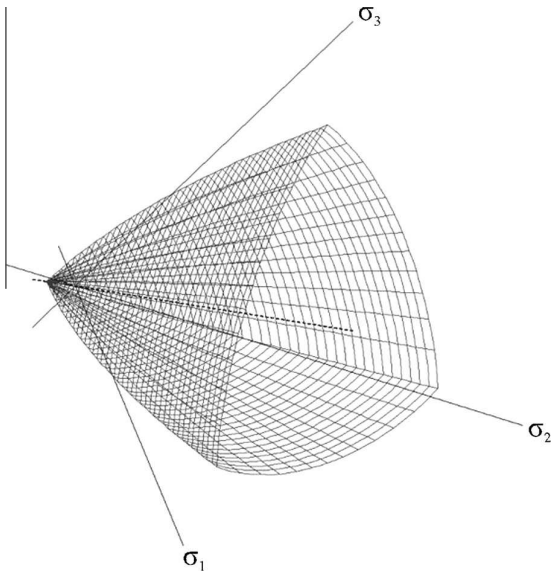

Fig. 6. Visualization of the three-parameter Menetrey and Willam [31] failure criterion (40).

In the above equations, (ξ,ρ,θ) are the Haigh–Westergaard stress coordinates and f_c and f_t are the compressive strength and tensile strength, respectively. Parameter $e \in (0.5,1.0)$ defines the roundness of the Menétrey-Willam failure surface, with a recommended value $e = 0.52$ [32]. The plastic surface is not constant. Its evolution is governed by the equivalent plastic strain ε_{eqp}

$$\dot{\varepsilon}_{eqp} = \min(\dot{\varepsilon}_{p1}, \dot{\varepsilon}_{p2}, \dot{\varepsilon}_{p3}) \tag{41}$$

where ε_{pi} is the ith component of the principal plastic strains. The hardening is modelled by adjusting the compressive strength $\widehat{f}_c$, while the softening is controlled through the parameter c

Hardening $\varepsilon_{eqp} \in \langle -\varepsilon_{cp}; 0\rangle$

$$\widehat{f}_c(\varepsilon_{eqp}) = f_{c0} + (f_c - f_{c0})\sqrt{1 - \left(\frac{\varepsilon_{cp} - \varepsilon_{eqp}}{\varepsilon_{cp}}\right)^2} \tag{42}$$

Softening $\varepsilon_{eqp} \in \langle -\infty; -\varepsilon_{cp}\rangle$

$$\begin{aligned} c &= \left(1 - \frac{w_c}{w_d}\right)^2, \quad w_c \in \langle -w_d; 0\rangle \\ c &= 0, \quad w_c \in (-\infty; w_d) \\ w_c &= (\varepsilon_{eqp} - \varepsilon_{cp})L_c \end{aligned} \tag{43}$$

In the formulas above, ε_{cp} is the value of the plastic strain when the compression strength f_c is reached in a uniaxial compression test. f_{c0}

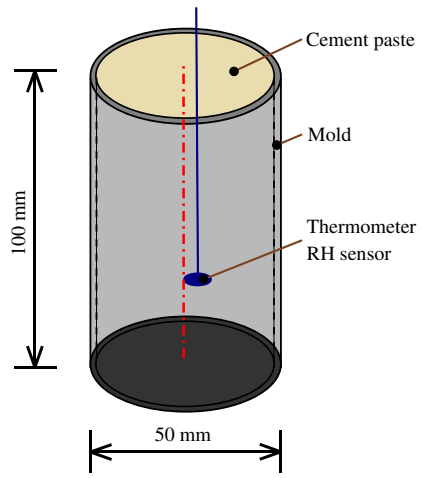

Fig. 8. Experimental setup for temperature and relative humidity measurement of cement pastes, $w/c = 0.25$ and $w/c = 0.50$.

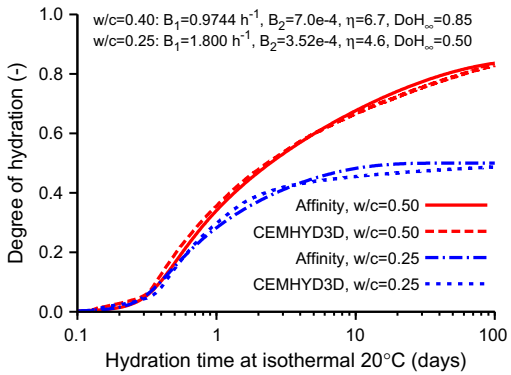

Fig. 9. Evolution of hydration degrees in cement pastes with w/c 0.25 and 0.50 from the CEMHYD3D model. The affinity model under isothermal 20 °C is fitted in.

is the onset of nonlinear behaviour in compression, w_d is the critical value of compressive displacement and w_c is the displacement when the compressive strength drops to zero. When concrete crushing enters into the softening regime, an analogous approach to the crack band model is also used for the localization in compression within the crushing band L_c. The crushing band L_c is calculated for each finite element as the element size projected into the direction of the minimal compressive stress (Fig. 7). This approach is based on the work of Van Mier [33], where it was experimentally shown that a unique value of the post-peak critical crushing dis-

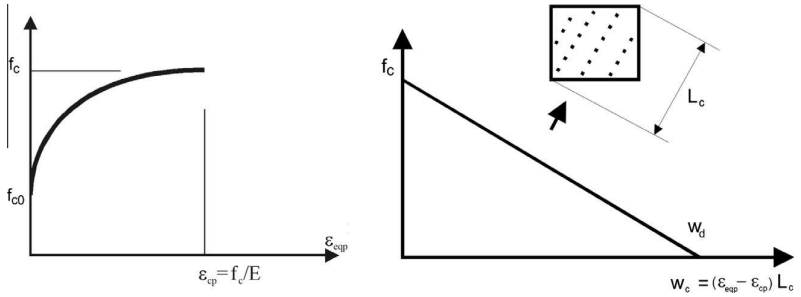

Fig. 7. Evolution laws for the plasticity model for concrete (left) hardening law, (right) softening law with crush band L_c definition.

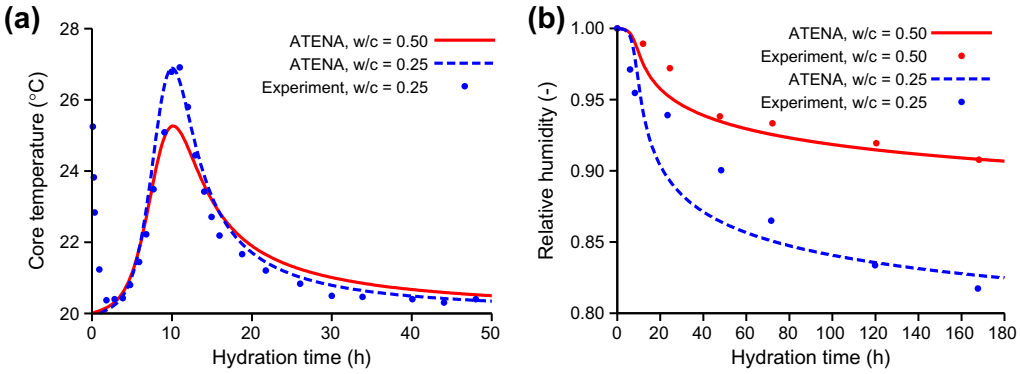

Fig. 10. Evolution of temperature and relative humidity of cement pastes.

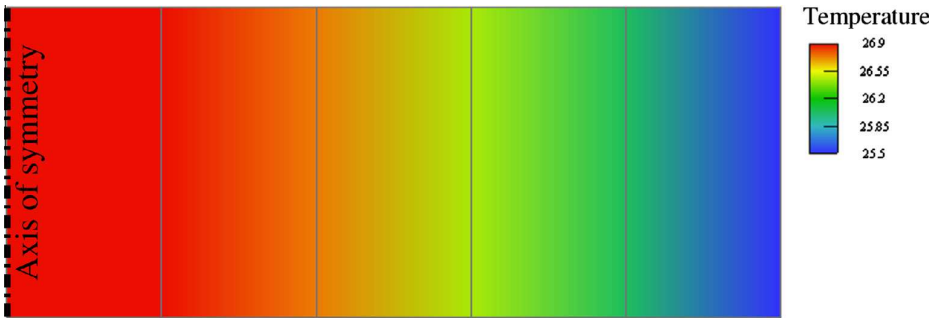

Fig. 11. Temperature field $T(\mathbf{x})$ at 10 h in radial direction, $w/c = 0.25$.

Fig. 12. Two arches of Oparno Bridge during construction (Photo by Jan L. Vítek).

placement w_d was recovered for the tested specimens independent of their sizes.

The plastic potential (45) defines the direction of the plastic flow, and is controlled by the parameter β, which defines the volumetric change during the crushing process: $\beta > 0$ means volume expansion, $\beta < 0$ material compaction, $\beta = 0$ material volume is preserved

$$G_p(\bar{\sigma}) = \beta\frac{1}{\sqrt{3}}I_1 + \sqrt{2J_2} \tag{44}$$

I_1 is the first invariant of stress vector and J_2 is the second invariant of deviatoric stress vector. The hardening/softening modulus H_p from (37) is defined as

$$H_p = \frac{\partial F_p}{\partial f_c}\frac{\partial f_c}{\partial \varepsilon_{eqp}}\frac{\partial \varepsilon_{eqp}}{\partial \lambda_p} + \frac{\partial F_p}{\partial c}\frac{\partial c}{\partial w_c}\frac{\partial w_c}{\partial \lambda_p} \tag{45}$$

The presented model is aimed to calculate plain and reinforced concrete structures. Any short-term one dimensional material law can be used for steel reinforcement, e.g. a multi-linear 1D model or an elasto-plastic model with hardening/softening.

3. Validation

The examples presented in this paper concentrate on the transport model and the combined hydro-thermo-mechanical model. The validation of the long-term and short-term mechanical models can be found in [26,34] and [28] respectively. The presented examples range from a low level cement paste experiment up to a benchmark study using a full multiscale formulation of the developed hydro-thermo-mechanical analysis.

3.1. Hydration of cement paste

Nawa and Horita [35] measured the temperature and moisture evolution in hydrating cement paste for several w/c's. Fig. 8 depicts the setup of the experiment. Numerically, the problem is modelled as a 1D axisymmetric case of hydro-thermal analysis. Heat conduction in the axial direction was neglected and the lateral heat transfer coefficient was set to $57500\,\mathrm{J\,h^{-1}\,m^{-2}\,K^{-1}}$ with external constant ambient temperature of 20 °C. It reflects the effect of the mould and the surrounding environment (see Fig. 8).

Table 1 summarizes all material input data for the w/c ratios of 0.25 and 0.5. The difference in hydration kinetics in both w/c has to be approximated with two sets of affinity model parameters. Fig. 9 shows fitting the affinity model to the CEMHYD3D simulation. The major difference between pastes with the both w/c ratios occurs

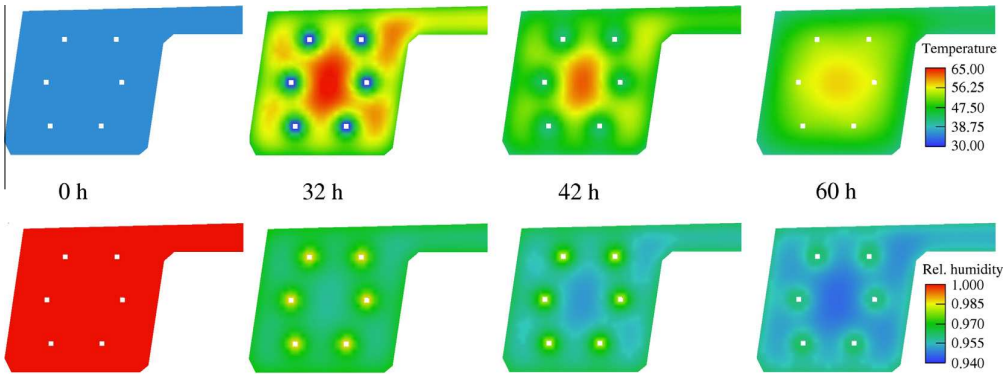

Fig. 13. Temperature (top) and relative humidity (bottom) fields in the left symmetric part of the arch cross section. The outer dimensions of the displayed cross-section are 3.5 × 2.17 m. Six cooling pipes are embedded.

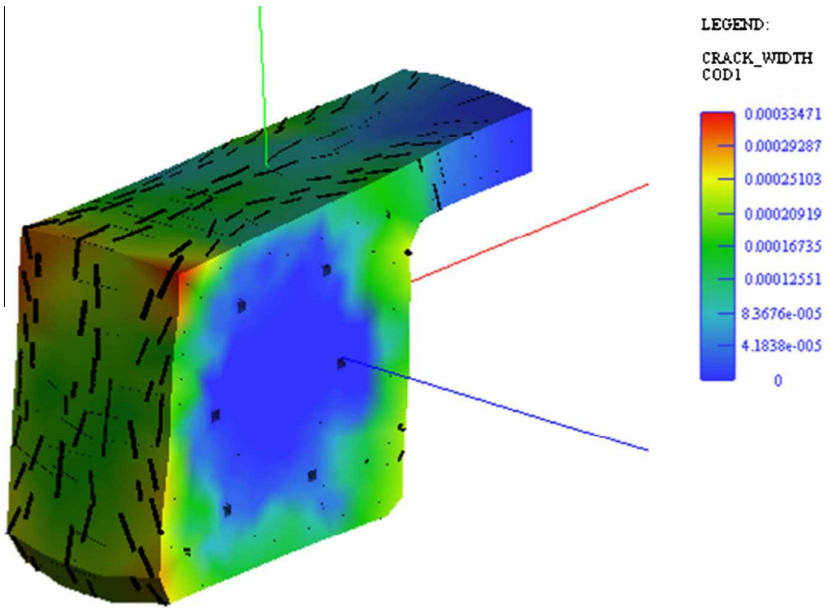

Fig. 14. Crack pattern in a 1 m long segment in Oparno Bridge.

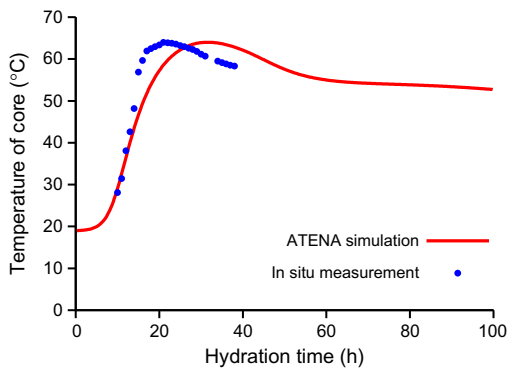

Fig. 15. Validation of the multiscale model on the Oparno Bridge arch.

Fig. 16. A validated massive RG8 beam with restrained shrinkage (image from the Cheops database).

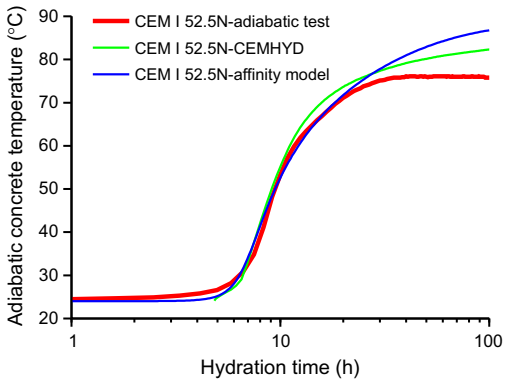

Fig. 17. Validation of the CEMHYD3D model and the affinity model in the concrete adiabatic test.

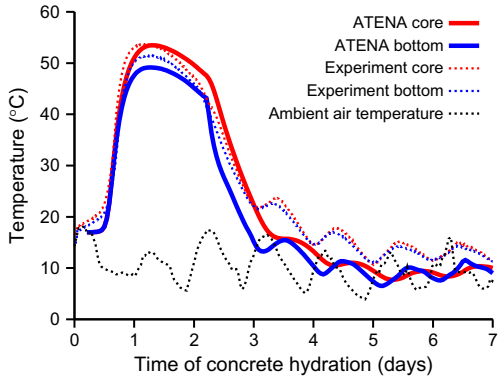

Fig. 19. Validation of the core and the bottom temperature.

after 1 day of hydration due to the depletion of available capillary water and capillary space in the case of $w/c = 0.25$.

Fig. 10 compares the evolution of the measured and calculated temperature and relative humidity. Fig. 11 displays the temperature field under the maximum core temperature at 10 h for the case of the sample with $w/c = 0.25$. The coupled model parameters in both pastes differ in the affinity hydration model, the cement and water content and in a different water mass at 80% relative humidity, see Table 1. The remaining parameters remain the same. It is worthy to note that although the model for moisture transport from Section 2.1.3 was derived for hardened concrete, it can be equally used for hydrating cement paste as is done here.

3.2. Arch of Oparno Bridge

A new reinforced concrete arch bridge was erected between 2008 and 2010. It is located on the Prague–Dresden highway. Two arches with a span of 135 m support pre-stressed bridge decks; see Fig. 12. They were designed with a special emphasis on durability and reduced maintenance costs, which in turn involved the need for temperature optimization during the casting. Thus, the procedure of casting aimed at reaching the minimum temperature during summer periods with feasible temperature gradients across selected cross sections.

Table 2
Mechanical time adjusted parameters for C50/60 concrete, $w/c = 0.475$.

Mechanical parameter at 28 days	Value
Cylindrical uniaxial compressive strength	50 MPa
Young's modulus	37 GPa
Compressive stress at the onset of cracking	4.1 MPa
Tensile strength	1.93 MPa
Fracture energy	48.3 J/m^2

The analyzed cross section is located above the scaffolding in Fig. 12. The left symmetric part has outer dimensions of 3.5×2.17 m. The analysis is treated as a 2D semi-infinite problem.

The most critical time for the temperature evolution occurred during the summer in 2009 with the top ambient air temperature over 30 °C. The C45/55 concrete composition was provided by the subcontractor and the evolution of hydration heat was simulated using the CEMHYD3D model. Thereafter, the affinity hydration model was calibrated. Table 1 summarizes concrete parameters for the simulation.

To avoid the development of excessive temperature within the arches, six cooling pipes were embedded in the half-cross section. After a few geometrical iterations, the most suitable position of the cooling pipes was found, see Fig. 13. The simulation revealed that cooling ice water could be turned off after about 40 h from the

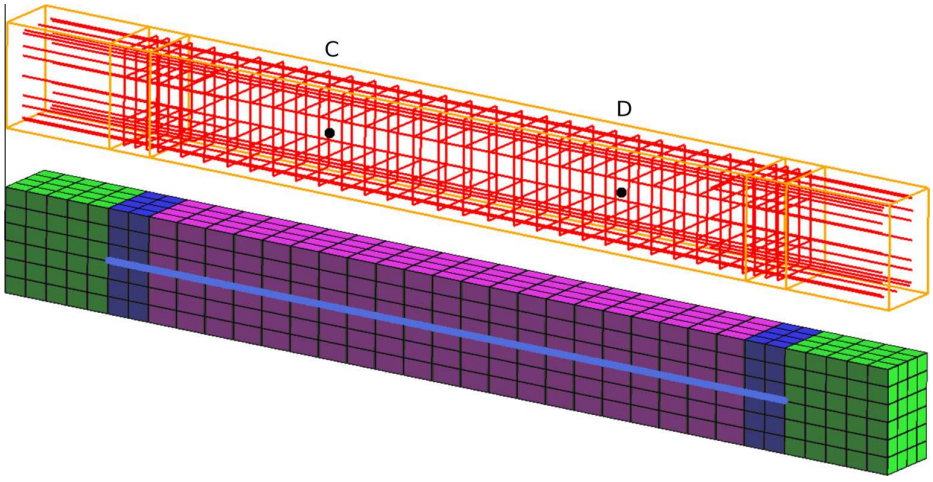

Fig. 18. Our model for RG8 showing the reinforcement, material assignment and points C, D with a mutual distance of 2.5 m on the beam axis.

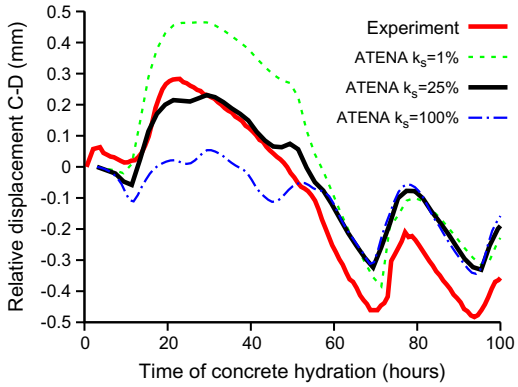

Fig. 20. Validation of relative displacements of points C–D. The coefficient k_s shows the stiffness reduction of the struts, where 25% is the most feasible value.

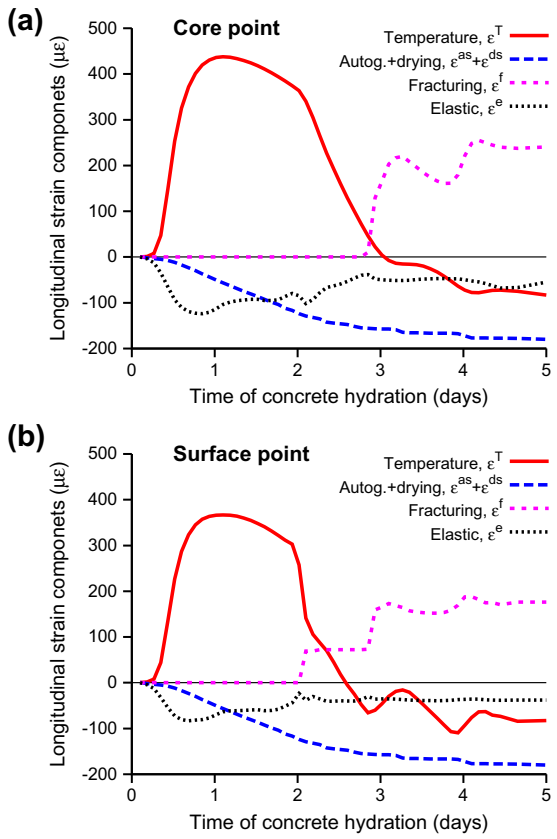

Fig. 21. Strain components in the core and surface point of the beam during hardening.

casting. Fig. 13 shows the temperature T and the moisture h fields at 0, 32, 42, 60 h of hydration. It was exercised that water cooling efficiently mitigated hydration heat and maintained the core temperature under 65 °C. Without water cooling, the maximum temperature would exceed 85 °C, which is unacceptable. The results of the transport analysis are added in Fig. 14 that shows a crack pattern caused by cooling of the outer surface.

The initial concrete temperature of the arch was set up to 19 °C, the ambient air temperature was kept constant at 21 °C and the temperature of the cooling water was maintained constant at 7 °C. The heat transfer coefficient on the concrete surface was estimated at 10 W m^{-2} K^{-1}. Note that the initial concrete temperature is one of the most sensitive factors in controlling the maximum core temperature.

Fig. 15 validates the simulation and shows a reasonable prediction. The small discrepancy is most probably due to a bit higher cement fineness, a continuous casting process and possibly variable initial temperature of mix batches.

3.3. RG8. experiment from ConCrack

The validation of the coupled hydro-thermo–hydro-mechanical analysis originates from the well-documented RG8 ConCrack benchmark experiment. For further information see http://www.concrack.org/. 18 teams modelled the RG8 beam and their results were gathered by the organizer during a blind stage. In the next feedback stage, the teams received their experimental data with the simulations. It was the starting point for the presented analysis.

Fig. 16 shows the overall geometry of the RG8 beam with two massive heads on both sides and two restraining steel struts. The central beam part has dimensions of 0.5 × 0.8 × 5.1 m and is reinforced. The benchmark experiment provides data on the cement mineral composition, cement fineness, concrete composition, reinforcement, geometry, external temperature, internal temperature in three points, adiabatic concrete temperature and displacements of two points C, D located on the beam axis 2.5 m apart, see Fig. 18.

In order to succeed in the simulation, the hydration model had to be first calibrated, see Table 1. Fig. 17 shows the results from the adiabatic experiment and the calibrated affinity hydration model.

The same finite element mesh was used for heat/moisture transport and mechanical analyses. It is shown in Fig. 18. Note that the beam's heads were simplified and the struts were tied directly to the surfaces of the central beam.

The beam had been initially insulated by a layer of 200 mm of expanded polystyrene. After 2 days of hydration the polystyrene was removed and thereafter the beam surface was exposed to the ambient air temperature and moisture. The original concrete composition stated 400 kg/m^3 of cement, which led to a temperature exceeding 70 °C in the adiabatic experiment. However, in reality, the maximum measured temperature was only 53.7 °C at 30 h of hydration. For this reason, we decided to reduce the clinker content to 320 kg/m^3. The potential energy of the clinker was 498.2 J/g of cement, see Table 1.

Fig. 19 validates the resulting temperatures in the bottom sensor located 50 mm above the surface and in the central part of the beam. Comparing the measured and calculated temperatures it can be found that the former ones are a bit higher, probably due to the additional supply of solar energy, which was neglected in the model. After approximately 4 days, the beam temperatures follow the fluctuations of ambient air temperature.

Relative humidity in the beam gradually decreases to 0.88, however, no experimental data were provided to validate this result.

The static creep analysis was carried out for times from 0.1 to 30 days. Table 2 summarizes the most important material parameters for C50/60 concrete used in the analysis. Note that they represent default values for concrete of this specification.

Autogeneous shrinkage calibrated from the measured data does not play a significant role due to a high $w/c = 0.475$. Creep and shrinkage related properties were predicted by the B3 material [27], updated with previously computed moisture and temperature fields.

In order to avoid complexity with additional reinforcement and transverse pre-stressed tendons in the heads, our model simplified the cantilever wings into which the struts are attached; compare Figs. 16 and 18. A direct connection to the beam was applied. How-

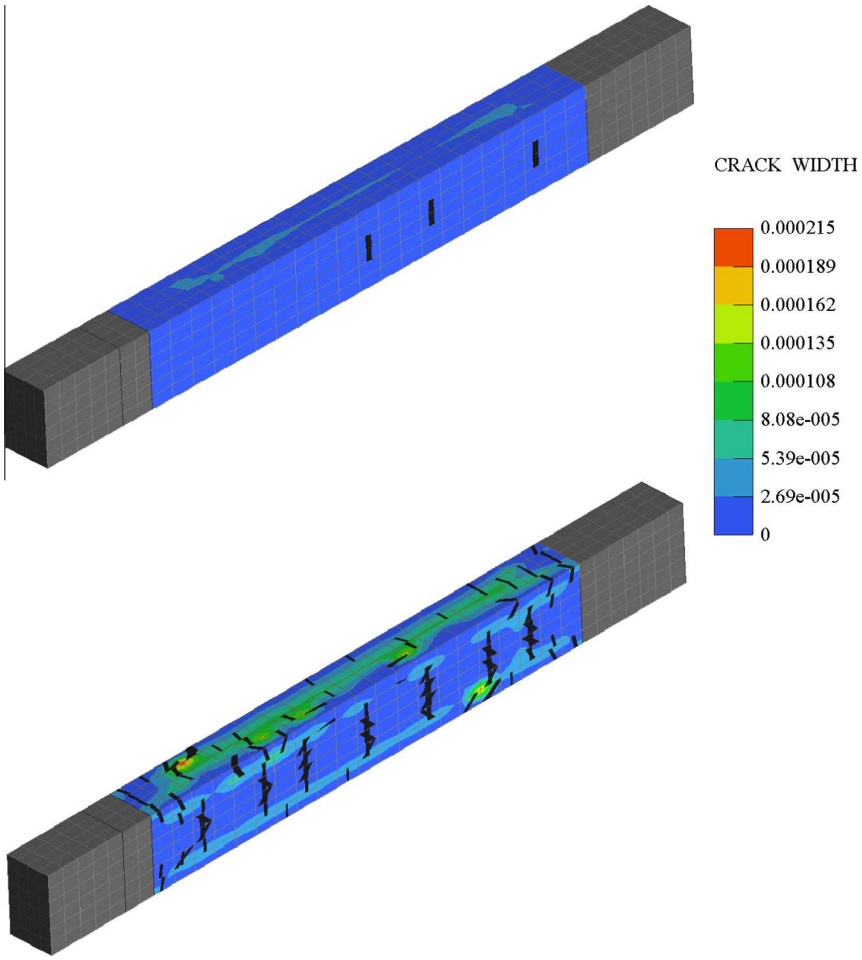

Fig. 22. Cracks in the beam at 75 h (the upper figure) and at 30 days (the bottom). Cracks below 150 micrometers are filtered out.

ever, as the wings increased the resulting compliance, we had to increase artificially the strut compliance. Let us consider the wings at the time of 0.6 day. Young's modulus at that time was 5 GPa. The original compliance of one separate strut was 0.777 mm/MN. Then, if we treat the wing as a cantilever beam, we get its total shear and bending compliance of 1.143 mm/MN. Therefore, the bracing effect of the original struts and wings can approximately be incorporated by reducing the original cross-section area of the model's struts A_s to $A_{s,reduced} = Ak_s$, where $k_s = 0.25$.

Fig. 20 shows displacements at control points C, D for different stiffness of the struts. It can be found that the stiffness reduction of the struts affects the displacement only up to about 3 days of hydration. Afterwards, the displacement of the points C, D follows the fluctuation of ambient air temperature due to material thermal expansion.

Fig. 21 displays the strain evolution during concrete hardening. When the sum of strains is positive, the concrete is under tension and fracturing strain is likely to be introduced. No plastic strain occurred during the calculation, which signalizes no concrete deterioration in compression. It is evident that temperature strain is the most important contribution at early ages.

Crack development in the beam is presented in Fig. 22. The experiment revealed that the first major crack occurred close to the beam's mid-span at 75 h. Our simulation also predicted the crack occurrence at that time but the location was different, see Fig. 22. This mismatch can be explained by the fact that stress–strain conditions along the longitudinal beam's axis are similar and thus cracks can localize anywhere.

At the age of 30 days the numerical model computed several major cracks. The experimental results also showed severe cracks at that time. The maximum calculated crack width rose to about 250 μm. Unfortunately, no experimental evidence exists to validate this value.

4. Conclusion

The presented thermo-hydro-mechanical model demonstrates the high potential for the design of massive reinforced concrete structures. The model is quite versatile and can assess structures with a wide variety of concrete mixtures, including concretes made from blended cements. Such concrete mixtures are widely used in massive elements due to their low hydration heat.

The developed model is based on a staggered solution strategy. Firstly, the transport analysis is carried out to calculate the evolution of structural moisture and temperature fields. Thereafter, the mechanical behaviour of the reinforced concrete structure is solved. It imports the result from the transport analysis to enhance the creep and shrinkage prediction. The analysis incorporates geometrical as well as material nonlinearities such as large displacements and rotations, material damage, or crack formation.

The model may seem to be too complicated for a practical use due to the fact that it uses a high number of material parameters. However, the executed calibration and validation revealed that most of them can be default values. In some rare cases they can be refined. A suitable user interface makes such an analysis simpler [25]. Due to a lack of unified benchmark experiments, comparison with other thermo-hydro-mechanical multiscale models [6–13] becomes cumbersome.

The model has been implemented in Advanced Tool for Engineering Nonlinear Analysis (ATENA) software and thus it can be widely used in civil engineering practise.

Acknowledgements

The presented work was carried out within the FR-TI1/612 project from the Ministry of Industry and Trade of the Czech Republic and the GAP105/10/2400 grant from the Czech Science Foundation.

References

[1] Nilsson M. Thermal cracking of young concrete. Partial coefficients, restraint effects and influence of casting joints [Thesis]. Lulea, Sweden: Lulea Univeristy of Technology; 2000.
[2] Neville AM. Properties of concrete. John Wiley & Sons Inc.; 1997.
[3] Wang C, Dilger WH. Prediction of temperature distribution in hardening concrete. In: Proceedings of international RILEM symposium thermal cracking in concrete at early ages; 1994. p. 21–8.
[4] Bentz DP. Transient plane source measurements of the thermal properties of hydrating cement pastes. Mater Struct 2007;40:1073–80.
[5] Park K, Jee N, Yoon I, Lee H. Prediction of temperature distribution in high-strength concrete using hydration model. ACI Mater J 2008;105:180–6.
[6] Smilauer V, Krejci T. Multiscale model for temperature distribution in hydrating concrete. Int J Multiscale Comput Eng 2009;7:135–51.
[7] Huang CX. The three dimensional modelling of thermal cracks in concrete structure. Mater Struct 1999;32:673–8.
[8] Estrada CF, Godoy LA, Prato T. Thermo-mechanical behavior of a thin concrete shell during its early age. Thin-Wall Struct 2006;44:483–95.
[9] Grasberger S, Meschke G. Thermo-hygro-mechanical degradation of concrete: from coupled 3d material modelling to durability-oriented multifield structural analyses. Mater Struct 2004;37:244–56.
[10] Faria R, Azenha M, Figueiras JA. Modelling of concrete at early ages: application to an externally restrained slab. Cem Concr Compos 2006;28:572–8.
[11] Hellmich C, Mang HA, Ulm FJ. Hybrid method for quantification of stress states in shotcrete tunnel shells: combination of 3D in situ displacement measurements and thermochemoplastic material law. Comput Struct 2001;79.
[12] Gawin D, Pesavento F, Schrefler BA. Hygro-thermo-chemomechanical modelling of concrete at early ages and beyond. Part I: hydration and hygro-thermal phenomena. Int J Numer Methods Eng 2006;67:299–331.
[13] Maekawa K, Ishida T. Long-term deformational simulation of PC bridges based on the thermo-hygro model of micro-pores in cementitious composites. Cem Concr Res 2011;41:1310–9.
[14] Cervenka V, Cervenka J, Jendele L. Atena program documentation, Part 1. Theory. Prague: Cervenka Consl.; 2000–2007.
[15] Kada-Benameur H, Wirquin E, Duthoit B. Determination of apparent activation energy of concrete by isothermal calorimetry. Cem Concr Res 2000;2:301–5.
[16] Cervera M, Oliver J, Prato T. Thermo-chemo-mechanical model for concrete. I: Hydration and aging. J Eng Mech ASCE 1999;125:1018–27.
[17] Bazant ZP, Najjar LJ. Nonlinear water diffusion in nonsaturated concrete. Mater Constr 1972;5:3–20.
[18] Hansen TC. Physical structure of hardened cement paste. A classical approach. Mater Constr 1986;114:423–36.
[19] Bentz DP. CEMHYD3D: A three-dimensional cement hydration and microstructure development modeling package. Version 3.0.: NIST Building and Fire Research Laboratory; 2005.
[20] Toolbox TE. <http://www.engineeringtoolbox.com/thermal-conductivity-d_429.html>.
[21] Ruiz J, Schindler A, Rasmussen R, Kim P, Chang G. Concrete Temperature Modeling and Strength Prediction Using Maturity Concepts in the FHWA HIPERPAV Software. 7th International Conference on Concrete Pavements Orlando (FL), USA2001.
[22] Kuenzel HM. Simultaneous heat and moisture transport in building components. 1D and 2D calculation using simple parameters. Stuttgart: Fraunhofer Inst. of Building, Physics; 1995.
[23] Bathe KJ. Finite element procedures in engineering analysis. Englewood Cliffs, New Jersey 07632: Prentice Hall, Inc.; 1982.
[24] Bazant ZP. Mathematical modeling of creep and shrinkage of concrete. New York: John Wiley & Sons; 1988.
[25] Bazant ZP. Prediction of concrete creep effects using age-adjusted effective modulus method. ACI J 1972;69(4):212–7.
[26] Jendele L, Phillips DV. Finite element software for creep and shrinkage in concrete. Comput Struct 1992;45(1):113–26.
[27] Bazant ZP, Baweja S. Creep and shrinkage prediction model for analysis and design of concrete structures: model B3. In: Al-Manaseer A, editor. Creep and shrinkage of concrete. ACI Special Publication; 1999.
[28] Cervenka J, Papanikolaou V. Three dimensional combined fracture-plastic material model for concrete. Int J Plast 2008;24:2192–220.
[29] De Borst R. Non-linear analysis of frictional materials [Thesis]. Delft: Delft University of Technology; 1986.
[30] Bazant ZP, Oh BH. Crack band theory for fracture of concrete. Mater Struct 1983;16:155–77.
[31] Hordijk DD. Local approach to fatigue of concrete [Thesis]. Delft: Delft University of Technology; 1991.
[32] Menetrey P, Willam KJ. Triaxial failure criterion for concrete and its generalization. ACI Struct J 1995;92:311–8.
[33] Van Mier JGM. Multi-axial Strain-softening of concrete, Part I: fracture. RILEM1986. p. 179–90.
[34] Jendele L, Bittnar Z. Computational aspects in thermo-hydro-mechanical analysis of porous media – Part ll. Practical implementation of creep and shrinkage analysis into FE software. In: Topping BHV, Bittnar Z, editors. Computational structures technology. Edinbourgh: Saxe-Coburg Publication; 2002. p. 183–96. ISBN 1-874672-16-4.
[35] Nawa T, Horita T. Autogenous Shrinkage of high-performance concrete. In: International workshop on microstructure and durability to predict service life of concrete structures, Sapporo, Japan; 2004.